optica

Limiting the incident NA for efficient wavefront shaping through thin anisotropic scattering media

HYUNGWON JIN, BYUNGJAE HWANG, SANGWON LEE, AND **JUNG-HOON PARK*** ⓘ

Department of Biomedical Engineering, Ulsan National Institute of Science and Technology (UNIST), Ulsan, 44919, Republic of Korea
*Corresponding author: jh.park@unist.ac.kr

Wavefront shaping holds great potential for high-resolution imaging or light delivery either through or deep inside living tissue. However, one of the biggest barriers that must be overcome to unleash the full potential of wavefront shaping for practical biomedical applications is the fact that wavefront shaping, especially based on iterative feedback, requires lengthy measurements to obtain useful correction of the output wavefront. As biological tissues are inherently dynamic, the short decorrelation time sets a limit on the achievable wavefront shaping enhancement. Here we show that for wavefront shaping in thin anisotropic scattering media such as biological tissues, we can optimize the wavefront shaping quality by simply limiting the numerical aperture (NA) of the incident wavefront. Using the same number of controlled modes, and therefore the same wavefront measurement time, we demonstrate that the wavefront shaped focus peak to background ratio can be increased by a factor of 2.1 while the energy delivery throughput can be increased by a factor of 8.9 through 710 μm thick brain tissue by just limiting the incident NA.

1. INTRODUCTION

Optical imaging holds unique strengths for direct observation of life and disease due to the high spatiotemporal resolution, molecular specificity, and safety of nonionizing radiation. For example, optical histopathology is currently the gold standard for the diagnosis of disease based on its specificity and high contrast. However, since biological tissues are highly scattering for visible wavelengths, applications of optical imaging for clinical use are mostly limited to histopathology slides, endoscopy, and ophthalmology where we have access to either thin, superficial, or transparent layers of tissue. Since the majority of our organs are located deep inside our body, the limited penetration depth is a major barrier in unleashing the full power of optical imaging for widespread clinical use.

As a part of the ongoing efforts to solve this problem, wavefront shaping has shown great potential in recovering diffraction-limited resolution even through multiple transport mean free paths in turbid media, where all of the information about the incident light is scrambled [1–6]. The concept is based on the fact that when absorption is negligible, multiply scattered light that originated from a point source can be sent back to its origin based on time reversal symmetry of Maxwell's equations [7]. If (1) we can generate a target feedback signal at the position of interest, (2) measure the distorted emanating wavefront, and (3) play back the phase conjugate of the measured wavefront, we can obtain a tight focus at the target position either through or deep inside turbid media. As this entire sequence of events is required for successful focusing, advances in each step can bring new innovations, such as enabling

new ways to tag light noninvasively at deeper depths [8–15], realizing new wavefront sensing methods [16–25], and faster wavefront shaping [26–31].

Of the various wavefront shaping methods, iterative feedback-based wavefront shaping has currently found the most applications due to its simplicity and robustness [4,32]. Iterative feedback-based wavefront shaping can be realized by generating a target feedback beacon that is localized in 3D space by utilizing coherence gating [33,34], nonlinear excitation [35–37], acousto-optic tagging [9,10], or photoacoustic signals [11]. Using the signal intensity from the beacon as feedback, the wavefront of the incident light is iteratively modulated to maximize the feedback signal which is equivalent to sensorless wavefront sensing. As most biological tissues are affected by movements due to breathing, blood flow, as well as direct motion of the animal, the wavefront optimizing speed is vital for iterative feedback-based wavefront shaping to be effective in a realistic environment [38–41].

Factors defining wavefront shaping efficiency can be understood by looking at the relation between the incident and output wavefronts though turbid media which is described by a transmission matrix. For diffusive media, where the transmission matrix elements are statistically independent and follow a circular Gaussian distribution, the target focus intensity through turbid media can be increased as [2]

$$\eta = \frac{\pi}{4}(N-1) + 1, \tag{1}$$

where η is the enhancement factor for the target focus and N is the number of controlled modes. This model is valid for thick turbid

media with thickness $D > l^*$, where l^* is the transport mean free path. To reconstruct a focus with sufficient quality for imaging or light delivery applications, we can see that a large number of modes have to be measured and controlled, which limits the iterative wavefront shaping speed.

To overcome such limitations, here we demonstrate that for highly anisotropic turbid media, the enhancement factor can be further optimized by simply controlling the NA of the incident wavefront. For anisotropic media with thickness smaller than a transport mean free path, the angle of the output scattered light is highly correlated with the incident angle. This is an important characteristic that can be exploited for a wide range of biomedical optics applications because scattering of biological tissues is also strongly forward directed with an anisotropy factor g typically above 0.9. Based on this property, we show that optimized wavefront shaping through 710 μm thick brain tissue can be achieved by simply limiting the NA of the incident wavefront. Due to the efficient wavefront shaping, we achieve a significant increase in signal-to-noise ratio (SNR) and contrast in imaging through thick brain tissue slices. As the wavefront shaping quality is achieved using the same number of controlled modes, or in other words the same measurement time, our work provides a new perspective to reducing the optimizing time for efficient wavefront shaping in biological applications.

2. METHODS

A. Anisotropic Scattering Samples

To validate speckle characteristics for anisotropic scattering media, we first performed experiments using custom-made highly forward scattering phantom samples. We immersed 1 μm polystyrene beads (refractive index 1.59) in 1.5% agarose (refractive index 1.33 ± 0.01) with various concentrations: 0.3%, 0.7%, 2%. We measured the scattering mean free paths of the generated samples per concentration by measuring the amount of transmitted ballistic light as a function of sample thickness (see Fig. S1 of Supplement 1). Based on Mie theory [42], the anisotropy factor of 1 μm polystyrene beads in water is 0.93 and the transport mean

free paths for the respective concentrations are expected to be 1028.6, 436.7, and 157.7 μm at our laser wavelength of 561 nm. Experimentally, the transport mean free paths were found to be 712.1, 296.0, and 136.2 μm, slightly shorter than the theoretical values. We believe that the slightly larger degree of turbidity is mostly due to some remaining microbubbles that were not fully removed during the sample preparation. All samples used for the following experiments were made with the same physical thickness of 120 μm according to approximately 0.17, 0.41, and $0.88l^*$ (transport mean free paths) for the respective concentrations.

Using the phantom samples with different scattering lengths but the same anisotropy factor, we first analyzed the differences in output speckle intensity. We focused the incident light onto the anisotropic scattering samples using an objective lens with 0.15 NA. To observe the generation of higher spatial frequencies upon multiple scattering, we used a detection objective lens with a higher NA of 0.5. The experiments were conducted under identical conditions where the illumination and detection objective lenses were aligned such that, without the scattering samples, a tight focus was imaged on the camera.

After placing the scattering samples, the resulting output speckles were considerably different although the same converging spherical wavefront was incident on the samples for all experiments (Fig. 1). For the optically thick anisotropic scattering media according to $0.88l^*$, the speckle intensity was distributed evenly and overfilled the camera field of view. For comparison, we also measured the output speckle for the same conditions using a diffusive sheet of white paper covered with three layers of nontransparent tape (thickness > 20 scattering mean free paths and in diffusive multiple scattering regime), which showed similar distributions. In contrast, as the optical thickness of anisotropic scattering media was reduced, the speckle intensity distribution became more confined showing correlations with the size of the original incident light [insets, Fig. 1(a)]. The correlations were more evident when analyzing the spatial frequency components of the speckles [Fig. 1(a)]. For the thicker anisotropic scattering medium corresponding to $0.41{\sim}0.88l^*$, the spatial frequency bandwidth of the speckles was diffraction limited corresponding
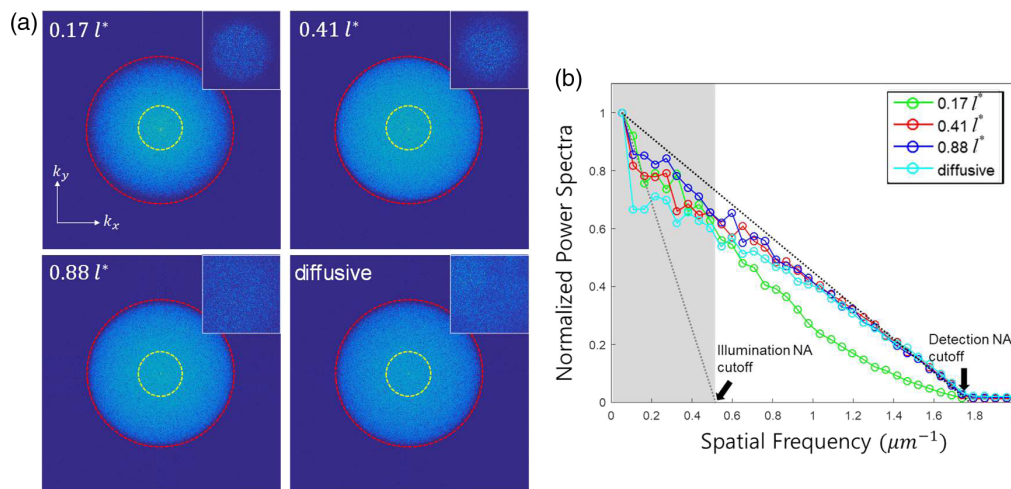

Fig. 1. Speckles generated through thin anisotropic scattering media are forward biased. (a) Log scale Fourier spectra of speckles measured through anisotropic scattering samples according to different l^*. "Diffusive" is a multiple scattering sample (layer of paper covered with three layers of nontransparent tape) for comparison. Yellow and red dotted circles correspond to the cutoff frequency of the incident and detection NAs, respectively. Insets show the measured speckles. (b) Normalized Fourier spectra radial distribution per sample. DC term has been omitted to remove baseline offset. Black dotted line: ideal MTF for the detection NA. Gray dotted line: ideal MTF for the illumination NA. Gray shaded area: spatial frequencies contained in the incident wavefront.

to the resolution limit of the detection NA. For thinner anisotropic scattering medium corresponding to $0.17l^*$, the speckles also showed an expansion in contained spatial frequencies but did not quite reach the full diffraction limit. More importantly, the Fourier amplitudes of the speckle intensities showed an important difference per sample turbidity. For the optically thick samples, the speckle intensity spatial frequency amplitude distribution showed a linear decrease with increasing spatial frequencies showing that the spatial frequencies of the random plane wave optical fields constituting the speckles have a nearly even amplitude distribution for the entire range of spatial frequencies captured by the detection NA. This is because for thick turbid media, the angular relation between the incident and output light is totally scrambled and the effective path length through the medium is irrespective of the incident direction and only dependent on the sample thickness. However, for optically thin anisotropic scattering media ($0.17l^*$), the spatial frequency spectra showed a faster decay for spatial frequencies beyond the incident light NA limit [Fig. 1(b)]. In this case, the directionality of the incident light is partially preserved and the effective optical path length through the thin anisotropic turbid medium is proportional to $\frac{L}{\cos\theta}$, where θ is the incident angle and L is the thickness of the medium. As such, for thin anisotropic scattering media, incident light with lower spatial frequencies undergoes a smaller number of scattering events and is transmitted through the medium more efficiently resulting in higher energy throughput.

Equation (1) assumed that speckles generated through multiple scattering are generated by statistically independent elements of the random transmission matrix following a circular Gaussian distribution [43]. Therefore, there is nothing to gain by selecting a specific distribution of input modes for wavefront shaping. All modes are statistically equivalent. However, we can see that for thin anisotropic scattering media, the transmission matrix elements connecting the low spatial frequency input modes have a greater influence on the output speckle field. Based on this observation, we hypothesized that by simply limiting the NA of the incident wavefront, and therefore selectively correcting for the transmission matrix elements that have relatively larger amplitudes, we can increase wavefront shaping efficiency using the same number of controlled modes. As a plus, we also expect that limiting the incident NA will not significantly limit the output wavefront resolution as we can still benefit from the spatial frequency bandwidth expansion due to multiple scattering in biologically relevant thin anisotropic scattering media.

B. Experimental Setup

For experimental validation, we utilized the geometry most widely used for bio-imaging, where the wavefront modulator is placed at a conjugate Fourier plane (Fig. 2). We conducted wavefront shaping experiments with the set of anisotropic scattering phantom samples mimicking properties of typical biological tissue as previously described (anisotropy factor 0.93, sample optical thickness 0.17, 0.41, $0.88l^*$). An adjustable iris was placed at the back focal plane of the incident objective lens to control the cutoff spatial frequency of the incident light. The incident laser (OBIS 561 nm, Coherent) power was calibrated and adjusted accordingly so that the same intensity was incident on the sample regardless of the iris size adjustments. The turbid medium was placed in front of the incident objective lens and a plane about 2.7 mm from the surface
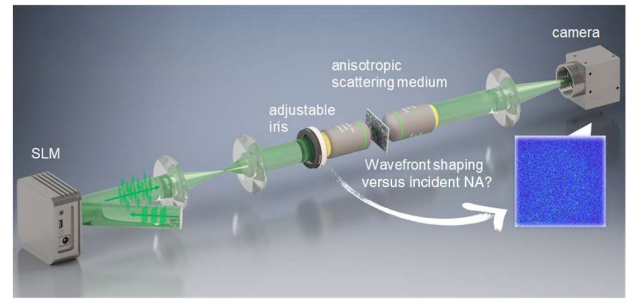
Fig. 2. Experimental setup schematic. An SLM placed at a conjugate Fourier plane shapes the incident wavefront. An adjustable iris placed at the back aperture of the illumination objective controls the incident NA. The output speckle is imaged by a camera.

of the turbid medium was imaged by the detection objective lens and tube lens pair onto a CMOS camera (Chameleon3, FLIR).

3. RESULTS AND DISCUSSION

A. Speckle Characteristics per Incident NA

It is well known that in contrast to adaptive optics, the size of the corrected focus for wavefront shaping is dependent on the detection NA rather than the controllable incident NA [44–48]. To quantify if this characteristic is valid for thin anisotropic scattering media, we first measured the output speckle intensity for different incident NAs. As seen in Fig. 3, the average speckle size varied slightly while the overall speckle distribution varied widely for different sample l^*. As the optical thickness reached close to a transport mean free path ($0.88l^*$), the output speckle overfilled the field of view (FOV) and displayed a homogeneous distribution regardless of the incident NA. The average speckle size also corresponded exactly to the diffraction limit as defined by the detection objective lens agreeing with characteristics of the diffusive sample. As the optical thickness of the anisotropic scattering media was decreased, the average speckle size increased to slightly above the diffraction limit. For the thinnest sample considered ($0.17l^*$, comparable to approximately $\sim 450\,\mu m$ thick chicken breast tissue [49]), the average speckle size was about 690 nm at full width at half-maximum (FWHM), 20% larger than the diffraction-limited point spread function FWHM ($0.51 \times \frac{\lambda}{NA_{det}} = 572$ nm) defined by the detection NA of 0.5. However, this average speckle size is still about 2.8 times smaller than the smallest focus that the illumination NA of 0.15 can generate ($0.51 \times \frac{\lambda}{NA_{ill}} = 1907$ nm) indicating that the speckle has undergone multiple scattering.

We report three important findings from this experiment. First, as we decrease the NA of the incident light, we observe that the average speckle intensity is concentrated toward the center of the FOV when the sample thickness is smaller than a transport mean free path (the overall directionality of light is partially preserved). This finding can have important practical implications. For instance, in phototherapy or optogenetics, this implies that simply reducing the illumination NA can deliver light more efficiently for target areas. Second, the transmittance is increased for lower incident NA for thin anisotropic scattering media. When applying the same laser intensity on the sample for different incident NAs, we find that the transmitted intensity increases for lower incident NAs. Third, due to multiple scattering, the average speckle size is smaller than obtainable using only the NA of the incident wavefront for all cases considered. Based on such observations,
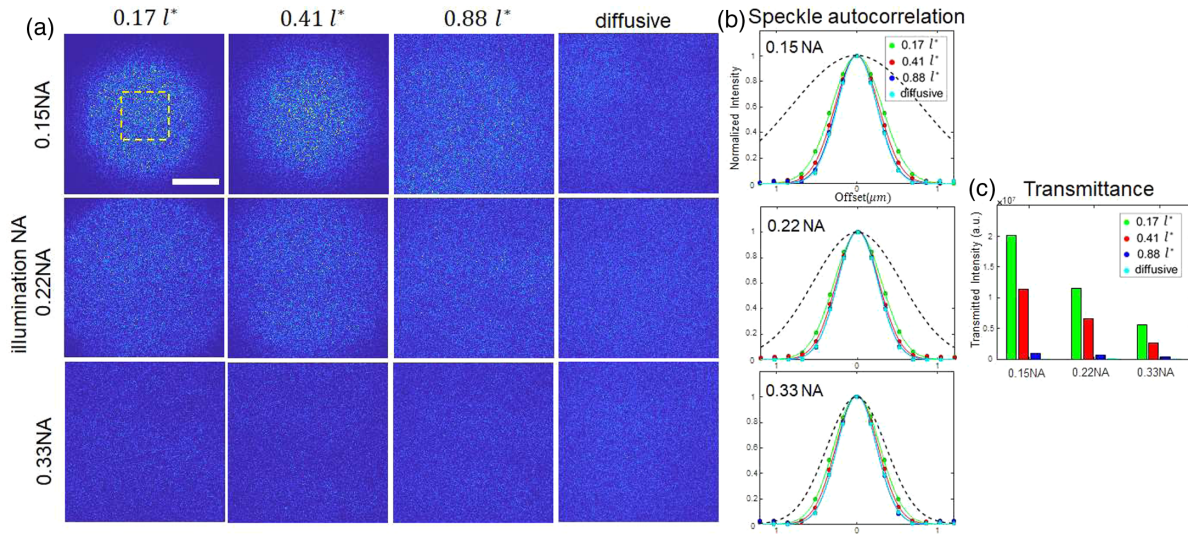
Fig. 3. Speckle characteristics per illumination NA and anisotropic scattering sample optical thicknesses. (a) For sample thickness $\geq l^*$, the speckles are evenly distributed overfilling the observable FOV regardless of the illumination NA. For thinner samples, the spread of the speckles is more focused for smaller incident beam NAs. Images have been normalized individually to clearly show the distribution of all speckles. (b) The average speckle size per each geometry was obtained by taking the normalized autocorrelation of the speckle intensity distribution. $0.88 l^*$ sample (dark blue) displayed the same speckle size as the diffusive sample (cyan) and perfectly matched the diffraction limit defined by the detection NA regardless of the incident NA. For optically thinner anisotropic samples the speckle size increased slightly for smaller illumination NAs. Black dotted lines show the diffraction-limited focus size as defined by the respective illumination NAs. (c) Transmitted light intensity measured in the central $52 \times 52\ \mu m^2$ region [dotted yellow square in (a)] when the same laser intensity is incident on each sample per incident NA. While the transmittance is nearly constant for the isotropic diffusive sample, thin anisotropic scattering samples display an increase in transmittance when limiting the incident NA. Scale bar, 50 μm.

we reasoned that in contrast to previous approaches in wavefront shaping, we can actually reduce the NA of the controlled incident wavefront to increase the enhancement factor for wavefront shaping through thin anisotropic turbid media using the same number of controlled modes. Ideally, the size of the obtained focus will not be severely compromised while the final obtained focus intensity can be significantly increased.

B. Incident NA Confined Wavefront Shaping

To validate such predictions, we performed wavefront shaping experiments through anisotropic scattering media using different incident light NAs. We utilized a frequency multiplexed analog phase modulation wavefront shaping scheme using a liquid crystal spatial light modulator (SLM, HSP512L, Meadowlark Optics) [50]. The SLM pixels were grouped into macropixels so that the incident light passing through the adjustable iris at the back focal plane of the objective lens was controlled by 316 spatial modes arranged in a circular shape. The phases of the individual modes were modulated at different frequencies and measured simultaneously to increase the SNR of our measurements. The multiplexed signals were separated by a temporal Fourier transform of the recorded intensity sequence and the correction wavefront was found by extracting the phase of the respective frequency components and displaying the phase conjugate of the retrieved phase on the according macropixels. In addition, the amplitude of the Fourier frequency components holds information about the relative contributions of the input modes on the corrected focus. We performed three iterations for each correction to ensure wavefront convergence [35]. The iterations gradually increase the SNR of the measurements and enable accurate wavefront shaping. Briefly, after a single iteration, an initial corrected focus is constructed. By keeping half of the SLM macropixels "on" with the obtained

correction wavefront, we can now use the corrected focus (albeit half the intensity) as the background reference to find the correction for the other half of macropixels. Since this reference signal is stronger than the average background speckle intensity prior to correction, we obtain an increase in SNR as each iteration increases the reference signal intensity. All experiments were conducted within the decorrelation times of the samples used.

Figure 4 shows the results for wavefront shaping through anisotropic turbid media. As previously discussed, the background speckle intensity also varies per incident light NA for thin anisotropic turbid media. The peak-to-background ratio (PBR) was defined as $\text{PBR} = \frac{I_{\text{focus}}}{\langle I_{bg\_c} \rangle}$, where I_{focus} is the intensity of the corrected focus and $\langle I_{bg\_c} \rangle$ is the ensemble average of the background speckle intensity (averaged over $19.3 \times 19.3\ \mu m^2$ area surrounding the focus) when the corrected wavefront is impinged on the sample. As expected, for diffusive media, the PBR and corrected focus size did not depend on the NA of the incident light [Fig. 4(a)]. In contrast, for anisotropic thin scattering media, the PBR varied widely for different incident NAs [Figs. 4(b)–4(d)]. For the $0.17 l^*$ thick anisotropic scattering sample, the PBR was increased by a factor of 2.5 simply by reducing the incident light NA from 0.33 to 0.15. This increase in correction efficiency cannot be explained by the possibility that the thin anisotropic sample only induced a small degree of aberrations that can have larger effects per correction mode (as in deploying adaptive optics for low-order aberrations). In fact, the correction wavefront shows a totally random phase distribution (Fig. 5) and the recovered focus is still surrounded by background speckles demonstrating that we are indeed in the multiple scattering regime rather than correcting for just low-order aberrations even for the optically thinnest sample currently considered.
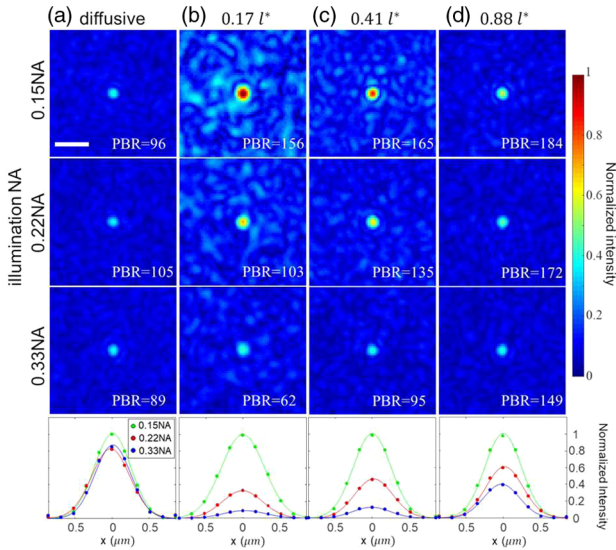
Fig. 4. Corrected foci as a function of sample optical thickness and NA of the incident wavefront. The images share the same color bar and have been contrast adjusted by a gamma correction factor of 0.35 to make the background speckles visible (see Fig. S2 of Supplement 1 for images in linear scale). (a) For diffusive media, the PBR is always similar irrespective of the illumination NA. (b)–(d) For anisotropic media, the PBR varies drastically for different incident NAs especially for thin anisotropic scattering media. The graphs show the focus intensity cross sections for the different NAs (normalized for each sample) illustrating the advantage of reducing the incident NA for efficient wavefront shaping in thin anisotropic scattering media. Scale bar, 3 μm.
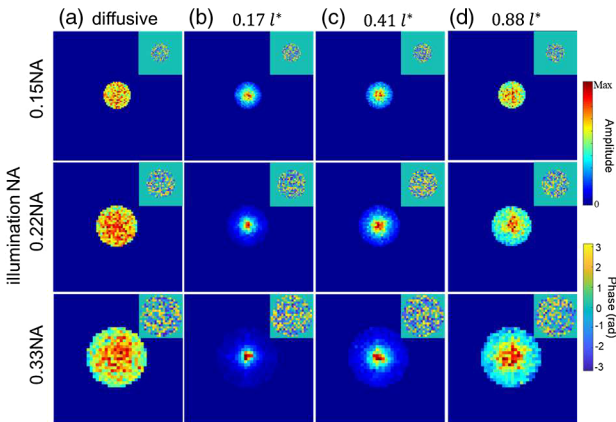
Fig. 5. Amplitude and phase of the transmission matrix components connecting the different incident modes to a single output mode (amplitude maps are average of $n = 10$ experiments). (a) For diffusive media, the amplitude of each transmission matrix element is nearly uniform regardless of the illumination NA. (b), (c) For thin anisotropic scattering media, transmission matrix elements show higher amplitude bias for lower spatial frequency input modes. (d) As the thickness is increased, the amplitude distribution of each transmission matrix component becomes more similar with the diffusive medium and evenly distributed showing that more input modes have similar contribution to the corrected focus. The corrected phase maps shown in the insets for all samples are random showing that multiple scattering is induced for all samples considered.

To understand the cause of the enhanced correction efficiency when limiting the NA of the incident light, we compared the amplitude profiles of the contribution of the individual controlled modes to the corrected focus. Using the transmission matrix formalism, we can describe our correction process by using the incident spatial frequencies as the input basis, and the output field pixels as the output basis. In our experimental geometry, each SLM macropixel corresponds to an input basis mode and each camera pixel corresponds to an output basis mode using this definition:

$$E_{\text{out},m} = \sum_{n=1}^{361} T_{mn} E_{\text{in},n}. \tag{2}$$

Here, $E_{\text{in},n}$ corresponds to the field generated by SLM macropixel n (amplitudes are constant and only phase is modulated), and T_{mn} is the element of the transmission matrix connecting the nth input mode to the mth output mode, $E_{\text{out},m}$. Successful focusing through turbid media is achieved by finding the correct $E_{\text{in},n}$ for all n, or in other words, the phase conjugate of the elements T_{mn}. Figure 5 shows the retrieved amplitude and phase of the measured correction through the iterative wavefront correction for the different experiments (amplitude maps are the average of $n = 10$ experiments; see Fig. S3 of Supplement 1 for individual results per wavefront shaping). Although hard to see in individual rounds of wavefront shaping, by averaging multiple experiments we can see a clear characteristic distribution of the transmission matrix amplitude profile. As only phase modulation is employed and the same amplitude is incident on the sample for all input basis modes (see Fig. S4 of Supplement 1), the average amplitude distribution for the measured correction wavefront should not show any bias for diffusive multiple scattering. We can see that for the diffusive medium, the amplitude distribution is indeed nearly uniform for all NAs of the incident light [Fig. 5(a)]. However, as the optical thickness is reduced for anisotropic scattering samples, the amplitude distribution is heavily concentrated toward lower incident spatial frequencies [Figs. 5(b)–5(d)]. In other words, the amplitudes of the transmission matrix elements are biased with larger amplitudes for smaller incident angles. Therefore, the assumption that the elements of the transmission matrix are randomly chosen from a circular Gaussian distribution is not valid for thin anisotropic scattering media and causes a deviation from Eq. (1).

Upon further analysis of the corrected focus and the remaining background speckle in thin anisotropic scattering media, we found another important different characteristic from diffuse random scattering. Due to macroscopic correlations, it has been shown that focusing through thick diffusive media also increases the background speckle intensity even when the wavefront correction is applied to only a single target output mode. However, this is a subtle phenomenon that is hard to observe in most experiments. In a typical wavefront shaping experiment, the average background speckle intensity is therefore usually considered to be constant regardless of the wavefront correction. However, when focusing through thin anisotropic scattering media, we observe that the background speckle intensity is considerably increased along with the corrected focus as we limit the incident NA (Fig. 6, also observable in Fig. 4).

Taking the surrounding background speckle intensity enhancement into account, the PBR cannot fully describe the characteristics of the wavefront correction. The enhancement factor η, which is nearly identical with the PBR for thick scattering media, can be used together with the PBR to describe the situation more clearly. We define the relative enhancement factor as $\eta_{\text{rel}} = \frac{I_{\text{focus}}}{\langle I_{bg\_b} \rangle}$, where I_{focus} is the intensity of the corrected focus and $\langle I_{bg\_b} \rangle$ is the
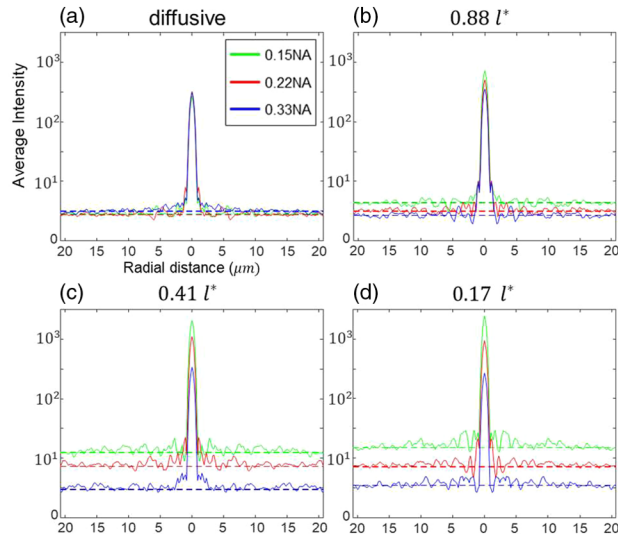
Fig. 6. Increasing energy throughput by limiting incident NA in thin anisotropic scattering media. Speckle intensities as a function of distance from the focus have been radially averaged. The radial averaged intensities are displayed symmetrically for visual aid. (a) For diffusive media, the wavefront shaped focus and associated background speckle are not dependent on the incident NA. (b) For anisotropic scattering media with $0.88l^*$ optical thickness, results are similar with thick diffusive media but increase in focus intensity as well as background speckle can start to be seen when limiting the incident NA. (c), (d) For thinner anisotropic scattering media, the effect is more evident. Importantly, both the background speckle and focus intensity increase by limiting the incident NA. Dotted lines show the average speckle intensity per incident NA before correction.

ensemble average of the background speckle intensity (averaged over $52 \times 52\ \mu m^2$ area surrounding the focus) before correction when illuminating the sample with the maximum NA of 0.33. The obtained focus size, η_{rel}, and PBR are shown in Table 1 for the different anisotropic scattering media optical thicknesses per illumination NA. We can clearly see that wavefront shaping with limited incident NA can increase the energy delivery throughput (η_{rel}) considerably while simultaneously increasing the contrast (PBR). This can find important applications where efficient delivery of light energy is important. For example, for phototherapy, increasing the total dose of illumination on the target deep inside biological tissue is one of the major remaining obstacles. To overcome this issue, research in developing novel agents that can utilize near-infrared radiation is gaining high interest due to more efficient light energy delivery into deep tissue. Our results suggest

that visible light, which has many more existing light-absorbing targets, can also be used more efficiently for phototherapy simply by employing wavefront shaping with intentionally reduced NAs. The target focus size is still nearly as sharp as when a large NA is used for wavefront shaping, but more importantly, the intensity of the focus and the surrounding speckles also increases for the same number of controlled modes so that phototherapeutic agents can be activated in an efficient manner.
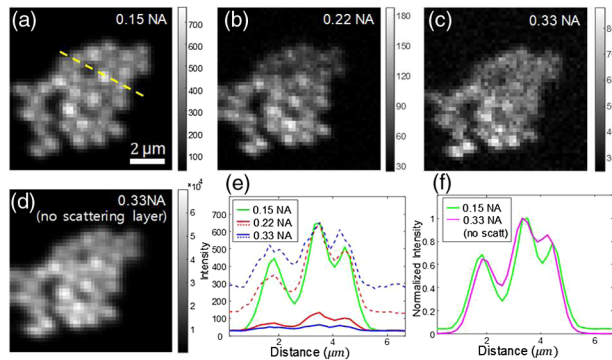
C. Imaging through Anisotropic Scattering Media

To demonstrate the advantage of using limited incident NA for optimized wavefront shaping in practical applications, we imaged 1 μm fluorescent beads through anisotropic scattering media made with polystyrene beads in agarose having $0.17l^*$ optical thickness. The fluorescent beads were placed on a translation stage to realize laser scanning-based imaging with the foci generated from wavefront shaping with different incident illumination NAs. The foci were first generated using the direct measurement of the transmitted speckle on the camera (Fig. 2). The fluorescent beads were then scanned over this focus. All experimental parameters except for the incident NA were kept identical. The imaging results using the wavefront shaped foci were drastically different for the different incident NAs [Figs. 7(a)–7(c)]. Defining the contrast as $C = \frac{I_{max} - I_{min}}{I_{max} + I_{min}}$, we find the contrast to be enhanced by 2.2-fold by simply constraining the illumination NA from 0.33 to 0.15. In addition, the maximum fluorescence intensity is increased by 10.5-fold [Fig. 7(e); also note the different range of color bars in Figs. 7(a)–7(d)]. Therefore, considering the system is shot noise limited, the SNR is automatically increased by $\sqrt{10.5} \approx 3.2$ fold. This clearly demonstrates that by simply using a smaller illumination NA for imaging through thin anisotropic media, we can obtain images with higher SNR and contrast. This enhancement in light delivery throughput may play a crucial role in successful light-induced treatment while using safe total light dosages. Another important aspect to note is that due to multiple scattering, the wavefront shaped foci exhibit higher resolution than the illumination NA. Due to this property, even though we restricted the illumination NA to enhance wavefront shaping efficiency, the resolution of the measured images was better than that obtained with the scattering sample removed and using a higher illumination NA [Figs. 7(d) and 7(f)].

To validate that our finding is valid for biological samples, we next imaged 1 μm beads through 710 μm thick fixed mouse brain tissue slice using the same imaging configuration (see Table S1 and Figs. S5 and S6 of Supplement 1 for wavefront shaping results for

Table 1. Focus Characteristics per Incident NA and Anisotropic Scattering Sample Optical Thicknesses, $n = 10$
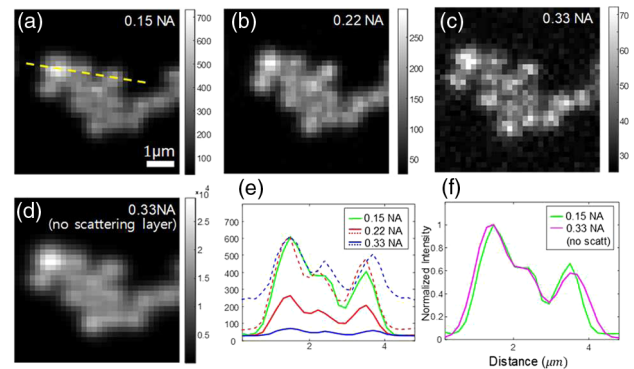
	$0.17l^*$			**$0.41l^*$**			**$0.88l^*$**		
NA_{ill}	0.15	0.22	0.33	0.15	0.22	0.33	0.15	0.22	0.33
FWHM(μm)	0.72 ± 0.04	0.67 ± 0.05	0.64 ± 0.03	0.60 ± 0.03	0.59 ± 0.02	0.58 ± 0.03	0.60 ± 0.02	0.58 ± 0.02	0.58 ± 0.03
PBR	145 ± 17.1	99 ± 11.3	59 ± 4.8	157 ± 17.7	140 ± 12.3	104 ± 12.5	180 ± 14.9	163 ± 17.9	147 ± 21.2
η_{rel}	833 ± 100.0	274 ± 35.4	64 ± 7.4	922 ± 139.8	434 ± 33.8	114 ± 11.5	397 ± 29.6	216 ± 16.6	153 ± 19.6

	diffusive		
NA_{ill}	0.15	0.22	0.33
FWHM(μm)	0.58 ± 0.03	0.59 ± 0.03	0.58 ± 0.03
PBR	90 ± 12.9	96 ± 15.5	96 ± 13.3
η_{rel}	81 ± 10.1	90 ± 11.2	79 ± 9.8

Fig. 7. Imaging through thin anisotropic scattering phantom. Laser scanning microscope images of fluorescent beads through anisotropic scattering medium after wavefront shaping using (a) 0.15, (b) 0.22, (c) 0.33 illumination NA. (d) Laser scanning microscope image with scattering phantom removed and using 0.33 illumination NA. System aberrations in the illumination beam have been corrected. (e) Line profile of the yellow dotted line marked in (a) for the different incident NAs (a)–(c). Dotted lines show the intensity normalized plots. Difference in contrast and signal level can be clearly seen. (f) Normalized line profile of the yellow dotted line marked in (a) for imaging with 0.15 NA incident through scattering phantom (a) and 0.33 NA with no scattering phantom (d).

Fig. 8. Imaging through brain tissue. Laser scanning microscope image of 1 μm fluorescent beads through 710 μm thickness of brain slice by wavefront shaping with (a) 0.15, (b) 0.22, (c) 0.33 illumination NA, and (d) laser scanning microscope image with brain tissue removed. (e) Line plot of yellow dotted line marked in (a) for the different incident NAs (a)–(c). Dotted lines show the intensity normalized plots. (f) Normalized line of profile the yellow dotted line for (a) and (d).

various brain slice thicknesses). All tissue samples were prepared in accordance with protocols approved by the Institutional Animal Care and Utilization Committee of UNIST. From the literature, the transport mean free path for mouse brain tissue slice is expected to be approximately 200 μm for the wavelengths currently used [51,52]. Therefore, 710 μm thick brain slice corresponds to about $\sim 3l^*$. Surprisingly, we can see that for brain slices, the advantage in limiting the incident NA for efficient wavefront shaping is retained for much thicker thicknesses than the phantoms we generated. We believe that this result may be due to higher degree of anisotropic scattering which has also been previously observed to extend the range of the optical memory effect for biological samples [52]. Simply constraining the illumination NA indeed increased the total light throughput as well as the focus PBR contrast for biological samples (Fig. 8). By reducing the illumination NA from 0.33 to 0.15, the maximum fluorescence intensity was enhanced by 8.9-fold while the contrast increased by 2.1-fold. The results are in good agreement with experiments conducted with the polystyrene bead phantoms. Considering that current state-of-the-art multiphoton imaging systems can reach over 500 μm depths in mouse brain tissue [53], our results indicate that wavefront shaping optimization by limiting the incident NA may be combined with such technologies to overcome current limits of deep tissue imaging. In addition, while we are exploiting the anisotropic scattering characteristics of biological tissue to optimize wavefront shaping efficiency, we still benefit from the favorable characteristics of multiple scattering. The wavefront shaped foci using 0.15 illumination NA shows similar or slightly better resolution than when using 0.33 NA with the brain tissue removed demonstrating resolution enhancement by over twofold by focusing through the brain tissue slice [Fig. 8(f)].

Having verified the effectiveness of our method in real biological tissues, we next performed wavefront shaped imaging experiments targeting intrinsic biological structures. Here we used a 180 μm thick mouse brain slice prepared from a Thy1-YFP-H transgenic mouse that was treated with secondary antibodies

labeled with Alexa Fluor 555 to enable fluorescence excitation from neurons compatible with our available laser source. To realize fluorescence imaging at this wavelength, we used a 532 nm continuous wave laser (SDL-532-100T, Shanghai Dream Lasers) and an emission filter (AT575lp, Chroma). All other experimental configurations were identical as previously described [a different SLM (Hamamatsu X10468-01) was used that, however, did not change experimental geometry]. We first performed wavefront shaping through the brain slice by using a camera in transmission geometry that was observing the laser speckle pattern on the opposite surface of the slice. We found that the size of the wavefront shaped foci varied for different brain areas depending on the relative turbidity. Here we chose an area where the FWHM of the wavefront shaped foci were obtained to be 900 nm and 1180 nm for incident NAs of 0.3 and 0.15, respectively, to obtain a comparatively large imaging field of view limited by the optical memory effect. The PBR values were 44 and 130, and η_{rel} were 39 and 555 for incident NAs of 0.3 and 0.15, respectively. The wavefront shaped foci were then scanned over a $14 \times 14\ \mu m^2$ area by applying appropriate linear phase ramps on the SLM, and emitted fluorescence intensity from the area according to the point spread function measured by the
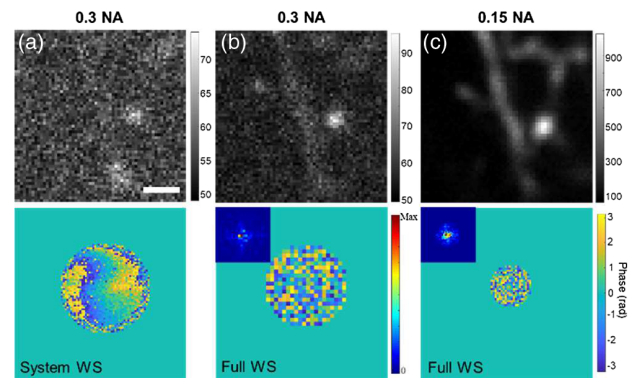
Fig. 9. Imaging intrinsic neuronal structures in a brain slice. (a) System aberration correction results in a noisy image where the brain structure is completely hidden below the baseline noise level. By performing wavefront shaping to correct for the sample induced disturbances, the brain structure can start to be seen using incident NAs of (b) 0.3 and (c) 0.15. The respective correction wavefronts are shown below. The corresponding amplitude maps are shown in the insets. Scale bar 3 μm.

camera in transmission geometry was used to reconstruct the images shown in Fig. 9. As seen in Fig. 9(a), correcting only for system aberrations results in an image dominated by noise with the fluorescence signal hidden below the noise floor. After wavefront shaping, the neuronal structures start to be visualized [Fig. 9(b)]. However, the image is still noisy due to the small signal level. To obtain higher-quality images, previous approaches required the control of additional modes to enhance the focus quality. In comparison, by simply limiting the incident NA, we can see that the image quality is significantly enhanced with the signal level increased by about an order of magnitude with the same number of controlled modes using our method [Fig. 9(c)].

D. Efficient Wavefront Shaping in Epi-Fluorescence Geometry

To further demonstrate that our method is applicable in general bio-imaging applications, we performed additional experiments in epi-fluorescence geometry. By using the same objective lens at the incident side of the scattering media for both wavefront shaping light modulation as well as fluorescence feedback signal detection, our method could be tested for general applicability with various epi-geometry-based biomedical optical techniques. For the following epi-fluorescence wavefront shaping experiments, an iris was placed in front of the SLM to control the incident beam size transmitted through the objective lens (see Fig. S7 of Supplement 1 for the experimental setup). As the iris was now placed at a conjugate Fourier plane instead of directly at the objective lens backpupil, the epi-fluorescence signal could be detected utilizing the full NA of the objective lens using a dichroic mirror while independently controlling the incident NA. An additional imaging system was configured past the scattering media in transmission geometry to verify the quality of the resulting wavefront shaped foci (which was not used during the wavefront shaping procedure).

Before performing wavefront shaping, we first checked if the incident NA was controlled accurately by removing the scattering medium and imaging the focus directly in transmission geometry. We found that the dichroic mirror (Semrock, FF573-Di01) caused severe aberrations [Figs. 10(a) and 10(b)] which, however, was easily corrected for via wavefront shaping (see Fig. S8 of Supplement 1 for wavefront shaping correction maps). For the incident NAs of 0.4 and 0.2, the corrected foci FWHM were measured to be 755 and 1474 nm in close agreement with theoretical diffraction-limited values.

Using a 1 μm fluorescent bead as the feedback beacon, we next performed wavefront shaping in epi-fluorescence geometry through the thin anisotropic scattering media made with polystyrene beads in agarose with $0.17l^*$ optical thickness. The total fluorescence intensity transmitted back through the scattering medium was integrated using CMOS1 placed in epi-geometry (Fig. S7 of Supplement 1). Using the total fluorescence intensity as feedback [54,55], we successfully obtained sharp foci for the different incident NAs [Figs. 10(c) and 10(d)]. Due to the energy delivery enhancement and optimized focus quality, the total fluorescence emission increases as well, which can be checked with CMOS1 [Figs. 10(e) and 10(f)]. We can clearly see that the increase in contrast and energy throughput by simply limiting the incident NA is also maintained in epi-fluorescence geometry (see also Table S2 of Supplement 1). Interestingly, the wavefront shaped foci FWHM using incident NAs of 0.4 and 0.2 were measured to be 620 nm and 680 nm, respectively, smaller than
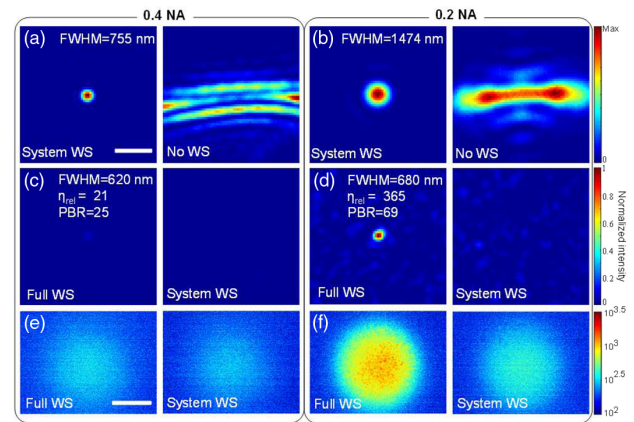
Fig. 10. Efficient wavefront shaping in epi-fluorescence geometry. Obtained focus without the scattering medium directly observed in transmission geometry using (a) 0.4 and (b) 0.2 incident NAs. Foci before and after system aberration correction (wavefront shaping, WS) are shown. (c), (d) Light transmitted through scattering medium before and after full WS for the respective incident NAs. While the focus sizes are both smaller than the perfect focusing without the scattering medium, the energy delivery throughput and contrast of the foci are drastically different. (e), (f) The fluorescence intensity as measured in epi-fluorescence geometry before and after wavefront shaping for the respective incident NAs. Scale bars, (a)–(d) 3 μm, (e), (f) 100 μm.

the diffraction limit defined by the detection NA of 0.4 used for the feedback signal measurements ($0.51 \times \frac{\lambda}{NA=0.4} = 715$ nm). Furthermore, this is also smaller than the 1 μm fluorescent bead used for feedback. Since the fluorescent beads have a homogeneous distribution of fluorophores packed inside their spherical volume and the Rayleigh range in our experiments is much longer than the size of the beads, we can think of the effective fluorescent beacon as a projection of the spherical fluorescence distribution onto a central plane. The wavefront shaping process then optimizes the light distribution that maximizes the light emitted from this fluorescence beacon. Theoretically, since the highest fluorescence density is concentrated at the center of the projected beacon, wavefront shaping will favor the sharpest focus that can be generated. In actual experiments, the limitation on the focus sharpness is decided by the diffuse area spreading of the speckles beyond the scattering medium and the distance to the target focus plane, and not dependent on the detection or illumination NAs. This is an interesting finding that suggests new directions in development of novel guide stars for wavefront shaping. Since the total excited fluorescence intensity is used for feedback, our observation demonstrates that not only the size but also the specific shape of the fluorescent beacon can be optimized and used as an additional design parameter to generate wavefront shaped foci with different properties tuned for various applications.

4. CONCLUSION

Recent advances in optical technologies have enabled visualization of life with unprecedented resolution and contrast revolutionizing biological studies at the research level. Unfortunately, the application of optical technologies at the clinical level is still severely limited mainly due to the multiple scattering problem [56,57]. Novel optical clearing methods have shown tremendous strength in this respect by directly removing the source of multiple scattering [58,59]. However, all optical clearing methods developed to

date require fixation of the sample and therefore are not compatible with live imaging or clinical applications.

Since the seminal work in 2007 by Vellekoop and Mosk [2], wavefront shaping has shown promise to be a truly noninvasive method enabling precise control of light at depths inside living tissue. However, one of the biggest remaining barriers for wavefront shaping has been the long measurement time required for accurate phase conjugation of the distorted wavefront. In this regard, previous works have focused on the development of novel techniques and hardware developments to speed up the process of the independent measurements required per controlled mode. Here, in a different perspective, we have demonstrated that for highly forward directional scattering media, such as biological tissue, the directionality of the incident light is partially preserved and can be taken to our advantage for efficient wavefront shaping. We demonstrated that by simply reducing the NA of the incident wavefront, we can enjoy a simultaneous increase in energy throughput and wavefront shaping efficiency with minimal loss in the resolution of the controlled output light. We showed the method to be effective in optimizing wavefront shaping through thick brain tissue, one of the most highly scattering biological structures. Since the method does not rely on any additional measurements or specialized hardware compared to conventional wavefront shaping schemes, the applicability of the method is generally broad and can be also combined with the recent developments in fast wavefront measurement techniques to obtain a synergistic boost in the wavefront shaping efficiency. We also demonstrated the method to be directly applicable in epi-fluorescence geometry, which can find a broad range of applications utilizing various previously developed optical tagging methods based on nonlinear, confocal, coherence, acousto-optic, or photoacoustic gating. We envisage that this new approach can open new avenues in a variety of biomedical applications where energy delivery enhancement or high-resolution imaging/photostimulation is required in a limited decorrelation time window or in light-starved environments.

Disclosures. The authors declare no conflicts of interest.

Supplemental document. See Supplement 1 for supporting content.

REFERENCES

1. A. P. Mosk, A. Lagendijk, G. Lerosey, and M. Fink, "Controlling waves in space and time for imaging and focusing in complex media," Nat. Photonics **6**, 283–292 (2012).
2. I. M. Vellekoop and A. P. Mosk, "Focusing coherent light through opaque strongly scattering media," Opt. Lett. **32**, 2309–2311 (2007).
3. R. Horstmeyer, H. Ruan, and C. Yang, "Guidestar-assisted wavefront-shaping methods for focusing light into biological tissue," Nat. Photonics **9**, 563–571 (2015).
4. I. M. Vellekoop, "Feedback-based wavefront shaping," Opt. Express **23**, 12189–12206 (2015).
5. S. Rotter and S. Gigan, "Light fields in complex media: Mesoscopic scattering meets wave control," Rev. Mod. Phys. **89**, 015005 (2017).
6. J.-H. Park, Z. Yu, K. Lee, P. Lai, and Y. Park, "Perspective: wavefront shaping techniques for controlling multiple light scattering in biological tissues: Toward in vivo applications," APL Photonics **3**, 100901 (2018).
7. Z. Yaqoob, D. Psaltis, M. S. Feld, and C. Yang, "Optical phase conjugation for turbidity suppression in biological samples," Nat. Photonics **2**, 110–115 (2008).
8. I. M. Vellekoop and C. M. Aegerter, "Scattered light fluorescence microscopy: imaging through turbid layers," Opt. Lett. **35**, 1245–1247 (2010).
9. Y. M. Wang, B. Judkewitz, C. A. Dimarzio, and C. Yang, "Deep-tissue focal fluorescence imaging with digitally time-reversed ultrasound-encoded light," Nat. Commun. **3**, 928 (2012).
10. X. Xu, H. Liu, and L. V. Wang, "Time-reversed ultrasonically encoded optical focusing into scattering media," Nat. Photonics **5**, 154–157 (2011).
11. F. Kong, R. H. Silverman, L. Liu, P. V. Chitnis, K. K. Lee, and Y. C. Chen, "Photoacoustic-guided convergence of light through optically diffusive media," Opt. Lett. **36**, 2053–2055 (2011).
12. E. H. Zhou, H. Ruan, C. Yang, and B. Judkewitz, "Focusing on moving targets through scattering samples," Optica **1**, 227–232 (2014).
13. C. Ma, X. Xu, Y. Liu, and L. V. Wang, "Time-reversed adapted-perturbation (TRAP) optical focusing onto dynamic objects inside scattering media," Nat. Photonics **8**, 931–936 (2014).
14. H. Ruan, T. Haber, Y. Liu, J. Brake, J. Kim, J. M. Berlin, and C. Yang, "Focusing light inside scattering media with magnetic-particle-guided wavefront shaping," Optica **4**, 1337–1343 (2017).
15. J. M. Yang, L. Li, A. A. Shemetov, S. Lee, Y. Zhao, Y. Liu, Y. C. Shen, J. W. Li, Y. Oka, V. V. Verkhusha, and L. H. V. Wang, "Focusing light inside live tissue using reversibly switchable bacterial phytochrome as a genetically encoded photochromic guide star," Sci. Adv. **5**, eaay1211 (2019).
16. S. M. Popoff, G. Lerosey, R. Carminati, M. Fink, A. C. Boccara, and S. Gigan, "Measuring the transmission matrix in optics: an approach to the study and control of light propagation in disordered media," Phys. Rev. Lett. **104**, 100601 (2010).
17. J. Yoon, K. Lee, J. Park, and Y. Park, "Measuring optical transmission matrices by wavefront shaping," Opt. Express **23**, 10158–10167 (2015).
18. I. M. Vellekoop, M. Cui, and C. Yang, "Digital optical phase conjugation of fluorescence in turbid tissue," Appl. Phys. Lett. **101**, 81108 (2012).
19. Y. Choi, T. R. Hillman, W. Choi, N. Lue, R. R. Dasari, P. T. So, W. Choi, and Z. Yaqoob, "Measurement of the time-resolved reflection matrix for enhancing light energy delivery into a scattering medium," Phys. Rev. Lett. **111**, 243901 (2013).
20. K. Lee, J. Lee, J. H. Park, J. H. Park, and Y. Park, "One-wave optical phase conjugation mirror by actively coupling arbitrary light fields into a single-mode reflector," Phys. Rev. Lett. **115**, 153902 (2015).
21. D. Akbulut, T. J. Huisman, E. G. van Putten, W. L. Vos, and A. P. Mosk, "Focusing light through random photonic media by binary amplitude modulation," Opt. Express **19**, 4017–4029 (2011).
22. A. Boniface, B. Blochet, J. Dong, and S. Gigan, "Noninvasive light focusing in scattering media using speckle variance optimization," Optica **6**, 1381–1385 (2019).
23. I. N. Papadopoulos, J.-S. Jouhanneau, J. F. A. Poulet, and B. Judkewitz, "Scattering compensation by focus scanning holographic aberration probing (F-SHARP)," Nat. Photonics **11**, 116–123 (2016).
24. A. Dremeau, A. Liutkus, D. Martina, O. Katz, C. Schulke, F. Krzakala, S. Gigan, and L. Daudet, "Reference-less measurement of the transmission matrix of a highly scattering material using a DMD and phase retrieval techniques," Opt. Express **23**, 11898–11911 (2015).
25. S. Kang, S. Jeong, W. Choi, H. Ko, T. D. Yang, J. H. Joo, J.-S. Lee, Y.-S. Lim, Q. H. Park, and W. Choi, "Imaging deep within a scattering medium using collective accumulation of single-scattered waves," Nat. Photonics **9**, 253–258 (2015).
26. C. Ma, F. Zhou, Y. Liu, and L. V. Wang, "Single-exposure optical focusing inside scattering media using binarized time-reversed adapted perturbation," Optica **2**, 869–876 (2015).
27. Y. Liu, C. Ma, Y. Shen, J. Shi, and L. V. Wang, "Focusing light inside dynamic scattering media with millisecond digital optical phase conjugation," Optica **4**, 280–288 (2017).
28. D. Wang, E. H. Zhou, J. Brake, H. Ruan, M. Jang, and C. Yang, "Focusing through dynamic tissue with millisecond digital optical phase conjugation," Optica **2**, 728–735 (2015).
29. D. B. Conkey, A. M. Caravaca-Aguirre, and R. Piestun, "High-speed scattering medium characterization with application to focusing light through turbid media," Opt. Express **20**, 1733–1740 (2012).
30. O. Tzang, E. Niv, S. Singh, S. Labouesse, G. Myatt, and R. Piestun, "Wavefront shaping in complex media with a 350 kHz modulator via a 1D-to-2D transform," Nat. Photonics **13**, 788–793 (2019).
31. K. Nam and J. H. Park, "Increasing the enhancement factor for DMD-based wavefront shaping," Opt. Lett. **45**, 3381–3384 (2020).

32. N. Ji, D. E. Milkie, and E. Betzig, "Adaptive optics via pupil segmentation for high-resolution imaging in biological tissues," Nat. Methods **7**, 141–147 (2010).

33. R. Fiolka, K. Si, and M. Cui, "Complex wavefront corrections for deep tissue focusing using low coherence backscattered light," Opt. Express **20**, 16532–16543 (2012).

34. J. Jang, J. Lim, H. Yu, H. Choi, J. Ha, J. H. Park, W. Y. Oh, W. Jang, S. Lee, and Y. Park, "Complex wavefront shaping for optimal depth-selective focusing in optical coherence tomography," Opt. Express **21**, 2890–2902 (2013).

35. J. Tang, R. N. Germain, and M. Cui, "Superpenetration optical microscopy by iterative multiphoton adaptive compensation technique," Proc. Natl. Acad. Sci. USA **109**, 8434–8439 (2012).

36. O. Katz, E. Small, Y. F. Guan, and Y. Silberberg, "Noninvasive nonlinear focusing and imaging through strongly scattering turbid layers," Optica **1**, 170–174 (2014).

37. J. H. Park, W. Sun, and M. Cui, "High-resolution in vivo imaging of mouse brain through the intact skull," Proc. Natl. Acad. Sci. USA **112**, 9236–9241 (2015).

38. M. Jang, H. Ruan, I. M. Vellekoop, B. Judkewitz, E. Chung, and C. Yang, "Relation between speckle decorrelation and optical phase conjugation (OPC)-based turbidity suppression through dynamic scattering media: a study on in vivo mouse skin," Biomed. Opt. Express **6**, 72–85 (2015).

39. A. M. Caravaca-Aguirre, E. Niv, D. B. Conkey, and R. Piestun, "Real-time resilient focusing through a bending multimode fiber," Opt. Express **21**, 12881–12887 (2013).

40. Y. Liu, P. Lai, C. Ma, X. Xu, A. A. Grabar, and L. V. Wang, "Optical focusing deep inside dynamic scattering media with near-infrared time-reversed ultrasonically encoded (TRUE) light," Nat. Commun. **6**, 5904 (2015).

41. M. M. Qureshi, J. Brake, H. J. Jeon, H. Ruan, Y. Liu, A. M. Safi, T. J. Eom, C. Yang, and E. Chung, "In vivo study of optical speckle decorrelation time across depths in the mouse brain," Biomed. Opt. Express **8**, 4855–4864 (2017).

42. S. Prahl, "Mie scattering calculator," retrieved https://omlc.org/calc/mie_calc.html.

43. J. W. Goodman, *Speckle Phenomena in Optics: Theory and Applications* (Roberts, 2007).

44. I. M. Vellekoop, A. Lagendijk, and A. P. Mosk, "Exploiting disorder for perfect focusing," Nat. Photonics **4**, 320–322 (2010).

45. G. Lerosey, J. de Rosny, A. Tourin, and M. Fink, "Focusing beyond the diffraction limit with far-field time reversal," Science **315**, 1120–1122 (2007).

46. J.-H. Park, C. Park, H. Yu, J. Park, S. Han, J. Shin, S. H. Ko, K. T. Nam, Y.-H. Cho, and Y. Park, "Subwavelength light focusing using random nanoparticles," Nat. Photonics **7**, 454–458 (2013).

47. Y. Choi, T. D. Yang, C. Fang-Yen, P. Kang, K. J. Lee, R. R. Dasari, M. S. Feld, and W. Choi, "Overcoming the diffraction limit using multiple light scattering in a highly disordered medium," Phys. Rev. Lett. **107**, 023902 (2011).

48. C. Ahn, B. Hwang, K. Nam, H. Jin, T. Woo, and J.-H. Park, "Overcoming the penetration depth limit in optical microscopy: Adaptive optics and wavefront shaping," J. Innov. Opt. Health Sci. **12**, 1930002 (2019).

49. D. L. Andrews, *Photonics, Volume 4: Biomedical Photonics, Spectroscopy, and Microscopy* (Wiley, 2015).

50. M. Cui, "Parallel wavefront optimization method for focusing light through random scattering media," Opt. Lett. **36**, 870–872 (2011).

51. L. Shi and R. R. Alfano, *Deep Imaging in Tissue and Biomedical Materials: Using Linear and Nonlinear Optical Methods* (CRC Press, 2017).

52. S. Schott, J. Bertolotti, J. F. Leger, L. Bourdieu, and S. Gigan, "Characterization of the angular memory effect of scattered light in biological tissues," Opt. Express **23**, 13505–13516 (2015).

53. J.-H. Park, L. Kong, Y. Zhou, and M. Cui, "Large-field-of-view imaging by multi-pupil adaptive optics," Nat. Methods **14**, 581–583 (2017).

54. I. M. Vellekoop, E. G. Van Putten, A. Lagendijk, and A. P. Mosk, "Demixing light paths inside disordered metamaterials," Opt. Express **16**, 67–80 (2008).

55. E. G. van Putten, A. Lagendijk, and A. P. Mosk, "Optimal concentration of light in turbid materials," J. Opt. Soc. Am. B **28**, 1200–1203 (2011).

56. A. Badon, A. C. Boccara, G. Lerosey, M. Fink, and A. Aubry, "Multiple scattering limit in optical microscopy," Opt. Express **25**, 28914–28934 (2017).

57. V. Ntziachristos, "Going deeper than microscopy: the optical imaging frontier in biology," Nat. Methods **7**, 603–614 (2010).

58. K. Chung, J. Wallace, S. Y. Kim, S. Kalyanasundaram, A. S. Andalman, T. J. Davidson, J. J. Mirzabekov, K. A. Zalocusky, J. Mattis, A. K. Denisin, S. Pak, H. Bernstein, C. Ramakrishnan, L. Grosenick, V. Gradinaru, and K. Deisseroth, "Structural and molecular interrogation of intact biological systems," Nature **497**, 332–337 (2013).

59. D. S. Richardson and J. W. Lichtman, "Clarifying tissue clearing," Cell **162**, 246–257 (2015).